JOURNAL OF SOLID STATE CHEMISTRY 120, 290–298 (1995)

Microdomains, Solid Solutions and the "Defect Fluorite" to C-Type Sesquioxide Transition in CeO_2–$RO_{1.5}$ and ZrO_2–$RO_{1.5}$ Systems

R. L. Withers,* J. G. Thompson,* N. Gabbitas,* L. R. Wallenberg,† and T. R. Welberry*

*Research School of Chemistry, Australian National University, Canberra, A.C.T., 0200, Australia; and †Inorganic Chemistry 2, Chemical Centre, University of Lund, P.O. Box 124, S-221 00 Lund, Sweden

Received June 9, 1995; accepted July 20, 1995

Satellite dark field (SDF) imaging is used to show that there is a definite change in symmetry on moving across the two-phase region separating the so-called "defect fluorite" and C-type sesquioxide solid solution regions in $(1-x)CeO_2 \cdot xRO_{1.5}$ and $(1-x)ZrO_2 \cdot xRO_{1.5}$ systems. SDF images of the "defect fluorite" side of the two-phase region are characterized by a microdomain texture on the ~100–200 Å scale and the local symmetry within any one of these microdomains is shown to be lower than cubic. Corresponding SDF images of the C-type sesquioxide side of the two-phase region are by contrast homogeneous and consistent with *Ia*3 space group symmetry. The nature of the local oxygen vacancy distribution on either side of the two-phase region is discussed and a possible model for the "defect fluorite" side of the two-phase region proposed. © 1995 Academic Press, Inc.

INTRODUCTION

The ability to adapt to quite large changes in the anion-to-cation ratio while maintaining the essential integrity of its FCC cation array is characteristic of many materials which exhibit the cubic, fluorite-type structure. The way in which such compositional flexibility is accommodated is a matter of continuing and considerable interest, both from the fundamental point of view of understanding wide-range, nonstoichiometric solid solutions and also because, at temperatures >~1000°C, such materials are usually anion-conducting, solid electrolytes. The oxides of a variety of trivalent metals, for example, can be reacted with ZrO_2 or CeO_2 at temperatures greater than ~1000°C to give oxygen-deficient, so-called "defect fluorite"-type solid solutions which typically exist over extraordinarily wide composition ranges (1). Indeed, in earlier papers on the ternaries $(1-x)CeO_2 \cdot xRO_{1.5}$, a continuous solid solution had been reported (2, 3) from $x = 0$ (fluorite-type, space group $Fm3m$, $a_F \sim 5.2$ Å, for CeO_2) all the way to $x = 1$ (C-type sesquioxide, space group $Ia3$, $a = 2a_F$, for $RO_{1.5}$).

The primary evidence for a continuous solid solution, apart from the apparently continuous variation in fluorite subcell lattice parameter as a function of composition, was the appearance of superlattice "reflections" characteristic of the C-type sesquioxide structure (at $\mathbf{G}_F \pm \frac{1}{4}\{220\}^*$, where $\mathbf{G}_F$ refers to the strong Bragg reflections of the underlying fluorite-type average structure) in X-ray powder diffraction (XRD) patterns, starting (weak and diffuse) at about 10–20 mole% $RO_{1.5}$ and increasing in intensity and sharpness with increasing concentration of $RO_{1.5}$ (2–4). The situation differs somewhat in the case of the $(1-x)ZrO_2 \cdot xRO_{1.5}$ systems in that the additional scattering accompanying the strong Bragg reflections of the underlying average structure changes quite significantly as a function of composition and only becomes localized in the vicinity of the $\mathbf{G}_F \pm \frac{1}{4}\{220\}^*$ regions of reciprocal space at sufficiently high concentrations of $RO_{1.5}$, typically for $x > \sim 0.5$ (5–7).

The two end-member, parent structure types (fluorite-type for ZrO_2 and CeO_2 and C-type sesquioxide for $RO_{1.5}$) are closely related. Their cation arrays are almost identical and the anions occupy tetrahedral sites in both cases—in fluorite-type ZrO_2 or CeO_2, all the available tetrahedral sites are occupied whereas in the C-type sesquioxide $RO_{1.5}$, only three-quarters of them (the 48(*e*) sites) are filled in a completely ordered array. The remaining one-quarter of the tetrahedral sites (the 16(*c*) sites) are unfilled at $x = 1$, ~30% filled at $x = 0.7$, and completely filled at $x = 0$ (8). At first glance, there seems to be no obvious reason why a continuous solid solution from fluorite- to C-type sesquioxide should not be possible.

Several decades ago, however, it was shown via accurate fluorite subcell lattice parameter measurements that there was always a two-phase region in the vicinity of 55–70 mole% $RO_{1.5}$ (9–11) separating a so-called "defect fluorite" solid solution from a C-type sesquioxide solid solution in such ternary systems. Given the apparent similarity of the superlattice on either side of the two-phase regions as judged by the existence of the same $\mathbf{G}_F \pm \frac{1}{4}\{220\}^*$ C-type superlattice reflections on either side (see Fig. 1), the ques-

0022-4596/95 $12.00

tion arises as to the structural origin of the miscibility gap. What has fundamentally altered from one side of the two-phase region to the other? Despite intensive investigation, the crystal chemistry underlying the existence of such two-phase regions has never been understood. It should be noted that the existence of such a two-phase region is not only characteristic of the ternary oxide systems which are the subject of the present study but also of binary oxide systems (where problems of cation mobility (9, 11), as occur in the case of these ternary systems, do not arise) such as in the PrO_{2-x}, CeO_{2-x}, and TbO_{2-x} systems at temperatures above ~1100°C (12).

The presence of apparent C-type superlattice reflections on the "defect fluorite" side of the two-phase region was originally interpreted as being due to microdomains or precipitates of essentially C-type structure (and $RO_{1.5}$ stoichiometry) embedded coherently into a fluorite matrix (of stoichiometry CeO_2 or ZrO_2 as appropriate). Such a model implies considerable cation compositional heterogeneity and, given the known slowness of cation diffusion at anything other than extremely high temperatures, might be expected to produce a strong dependence of experimental results (such as subcell lattice parameter measurements) upon conditions of synthesis. Protracted annealing experiments between 1500 and 1700°C, however, showed that such systems can be reversibly moved from the defect fluorite or C-type region into the two-phase region and back again (9). This is not what would be expected for a "diphasic" texture of C-type domains dispersed in a fluorite matrix. Similarly the systematic variability in relative intensity of second-order $\mathbf{G}_F \pm 2.\frac{1}{4}\{220\}^*$ to first-order $\mathbf{G}_F \pm 1.\frac{1}{4}\{220\}^*$ harmonic satellite reflections right across the defect fluorite and C-type solid solution fields is also incompatible with such an embedded C-type precipitate interpretation (see Fig. 1 and Ref. (4)), and it is clear that an alternative explanation must be found for the existence of supposedly C-type satellite reflections on the defect fluorite side of the two-phase region.

Withers *et al.* (13) and Suzuki *et al.* (14) have proposed a modulation wave approach to the defect fluorite side of the two-phase region whereby the local space group symmetry depends upon the number of primary $\frac{1}{4}\{220\}^*$-type modulation waves locally excited and their relative phase relationships. In the former, the primary $\frac{1}{4}\{220\}^*$ modulations were associated with oxygen vacancy ordering and associated structural relaxation while the second harmonic $\{001\}^*$-type modulations were associated with metal atom ordering and associated relaxation. In the latter, however, both primary and second harmonic modulation waves were proposed to be independent of any oxygen vacancy ordering and to involve only oxygen atom shifts.

In an earlier, largely HRTEM, study of the $(1 - x)CeO_2.xYO_{1.5}$ system (4, 13), no evidence was found for lowering of the local space group symmetry from the *Ia*3 space group symmetry of the type-C structure (with $a_C = 2a_F$) on either side of the two-phase region. Such a space group symmetry implies the simultaneous local existence of all six distinct $\frac{1}{4}\{220\}^*$-type modulation waves. On the other hand, Suzuki *et al.* (14) suggested that only one of the six possible $\frac{1}{4}\{220\}^*$-type modulation waves locally exists on the defect fluorite side of the two-phase region and that therefore six microdomains should be present with an equal probability. No direct evidence, however, was presented for this model. In this contribution we report clear evidence (obtained via satellite dark field imaging) for the existence of ~100 Å microdomains of lower local symmetry than cubic on the defect fluorite side of the two-phase region for both $(1 - x)CeO_2.xYO_{1.5}$ and $(1 - x)ZrO_2.xRO_{1.5}$ systems.

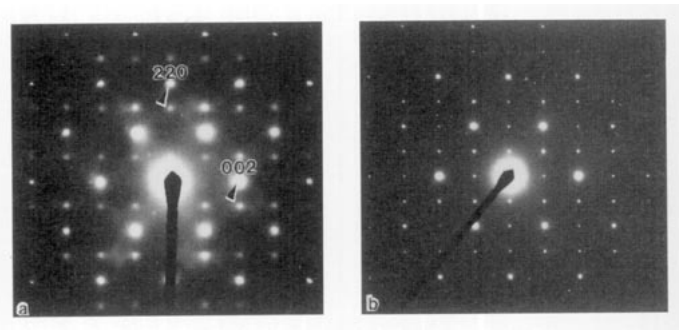

FIG. 1. Shows ⟨110⟩-type zone axis selected area electron diffraction patterns (SADPs) taken on the (a) defect fluorite and (b) C-type side of the defect fluorite to C-type two-phase region in the $(1 - x)ZrO_2.xHoO_{1.5}$ system. Indexing is with respect to the underlying fluorite-type average structure.

EXPERIMENTAL

Specimens of $(1 - x)CeO_2.xYO_{1.5}$ were prepared on either side of and within the two-phase region at 49.7, 64.8, and 79.8 mole% $YO_{1.5}$ (see (8) for details of specimen preparation). The 49.7 mole% $YO_{1.5}$ specimen was in the so-called defect fluorite-type solid solution and the 79.8 mole% $YO_{1.5}$ specimen was in the C-type solid solution. The 64.8 mole% $YO_{1.5}$ was grown within the two-phase region in the hope of obtaining a single-crystal specimen of either end member as the result of compositional unmixing and to determine the boundaries of the two-phase region. Specimens of $(1 - x)ZrO_2.xRO_{1.5}$, R = Ho, Dy, Tb, and Gd, were prepared both within the defect fluorite-type solid solution at 65 mole% as well as at 75 mole% within the two-phase region (see (6) for details of specimen preparation).

Specimens were finely ground in a mortar and pestle and then dispersed on a holey carbon grid for examination in JEOL 100CX, Philips EM 430, and JEOL 4000EX transmission electron microscopes.

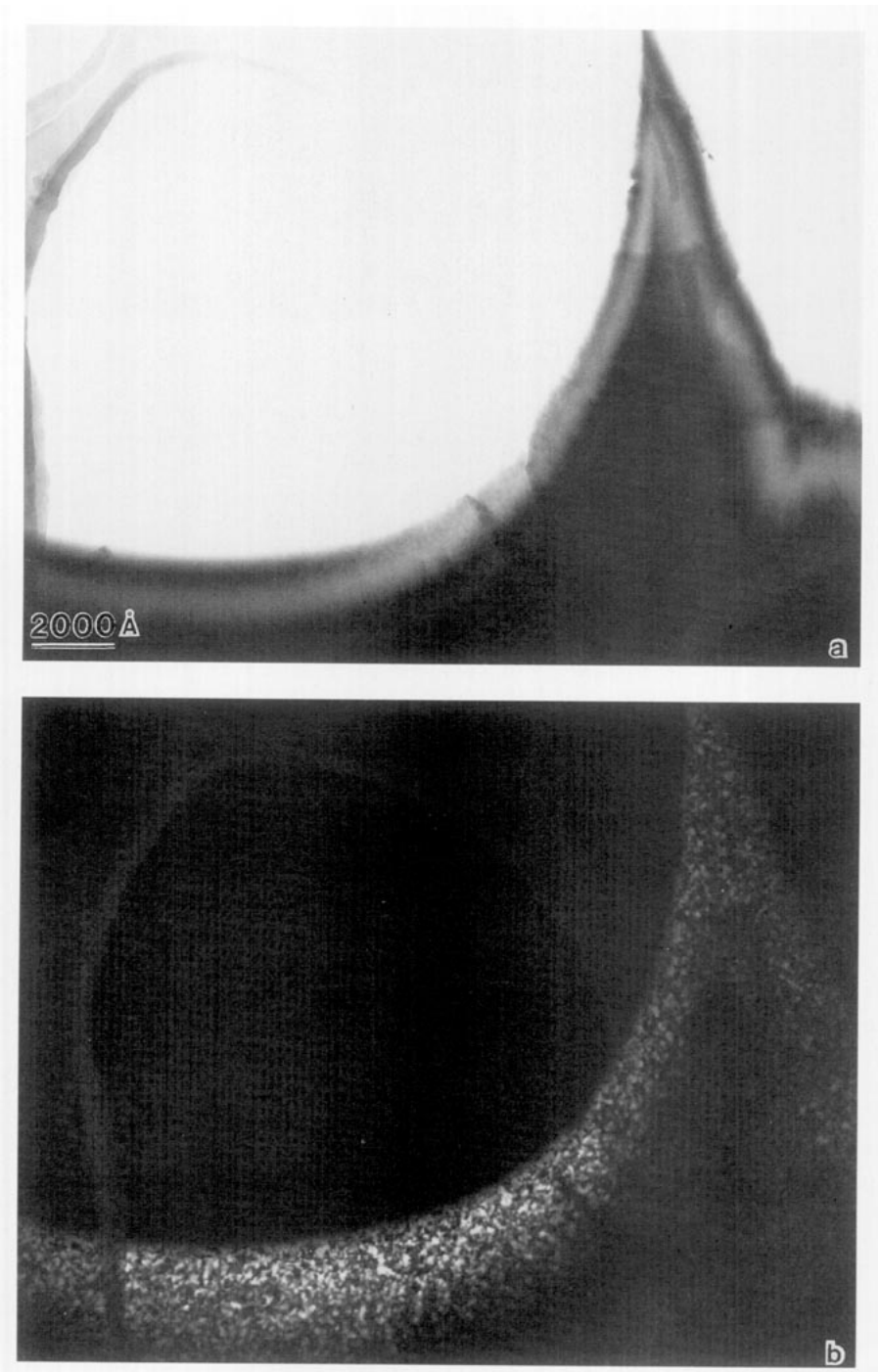

FIG. 2. An (a) bright field and (b) corresponding satellite dark field image (taken using a $\{11\bar{1}\}^* + \frac{1}{4}\{20\bar{2}\}^*$ satellite reflection in the close vicinity of a ⟨335⟩ zone axis orientation) of the 49.7 mole% $YO_{1.5}$ in CeO_2 specimen. The mottled microstructure of (b) is absolutely characteristic of the defect fluorite side of the two-phase region whenever a strongly excited $\mathbf{G}_F \pm \frac{1}{4}\{220\}^*$ satellite reflection is used to form a dark field image.

RESULTS

The microstructure visible in the satellite dark field (SDF) image of the 49.7 mole% $YO_{1.5}$ in CeO_2 specimen shown in Fig. 2b (and taken using a $\{11\bar{1}\}^* + \frac{1}{4}\{20\bar{2}\}^*$ satellite reflection in the close vicinity of a ⟨335⟩ zone axis orientation) is absolutely characteristic of the defect fluorite side of the two-phase region whenever a strongly excited $\mathbf{G}_F \pm \frac{1}{4}\{220\}^*$ satellite reflection is used to form a dark field image. The corresponding bright field (BF) image of Fig. 2a shows no such characteristic microstructure. Similar SDF images showing the same characteristic mottled mi-

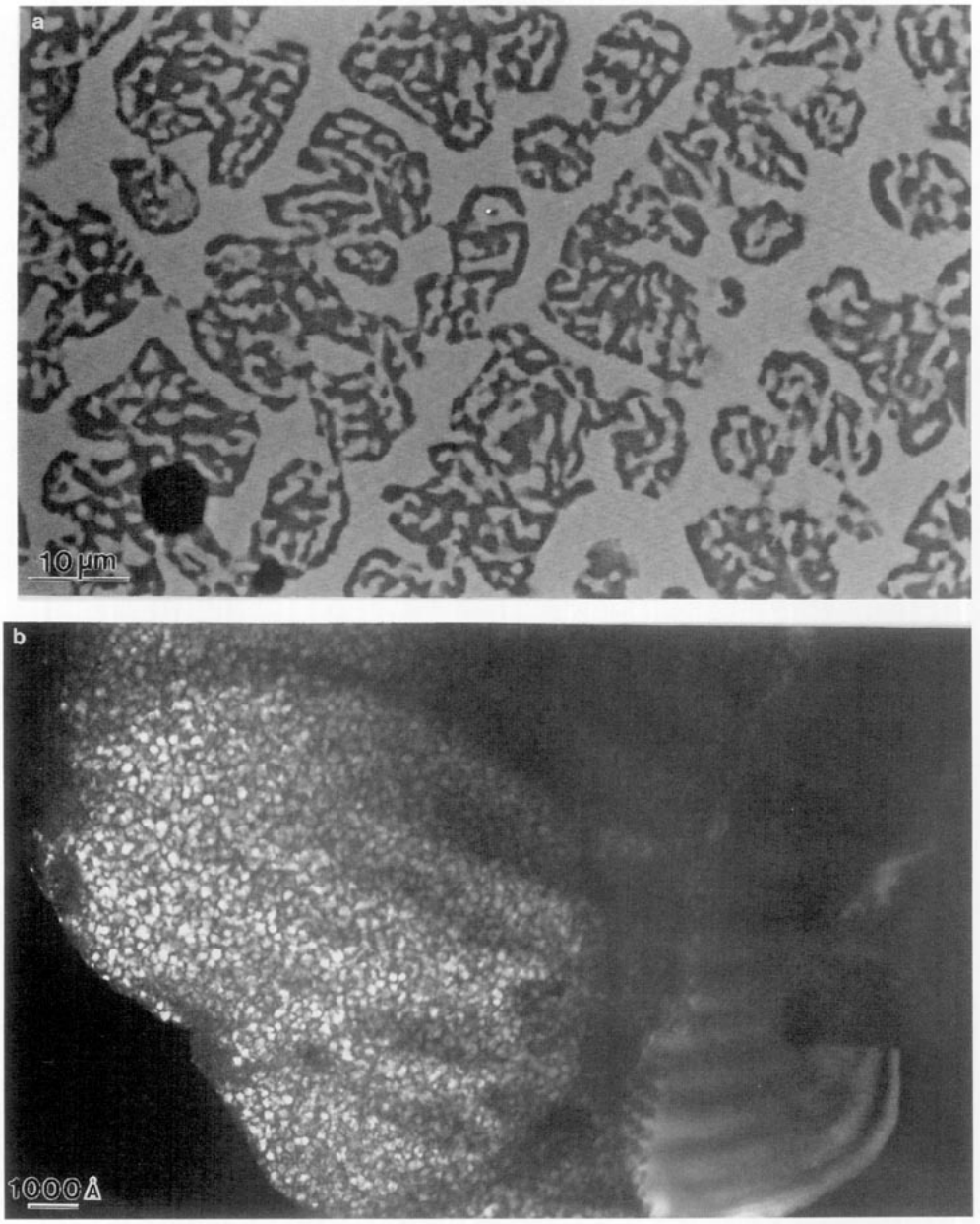

FIG. 3. (a) A back-scattered electron image of a 64.8 mole% $YO_{1.5}$ in CeO_2 specimen showing unmixing of the C-type and defect fluorite-type solid solutions on the micrometer scale. The darker regions correspond to the ~73 mole% $YO_{1.5}$, C-type side of the two-phase region, whereas the lighter regions correspond to the ~50 mole% $YO_{1.5}$, defect fluorite side of the two-phase region. (b) A higher resolution, $\mathbf{G}_F \pm \frac{1}{4}\{220\}^*$ SDF image taken tilted ~5–10° away from an ⟨001⟩ zone axis orientation of a grain of the same specimen. The right-hand side of the grain corresponds to the C-type side of the two-phase region and shows absolutely no evidence for a microdomain texture, whereas the left-hand side of the grain corresponds to the defect fluorite side of the two-phase region and shows clearly the existence of microdomains on the 100–200 Å scale.

crostructure have also been obtained from each of the $(1 - x)ZrO_2.xRO_{1.5}$, R = Ho, Dy, Tb, and Gd, specimens on the defect fluorite side of the two-phase region and show that the amplitude of the particular $\frac{1}{4}\{220\}^*$ modulation wave giving rise to the $\mathbf{G}_F + \frac{1}{4}\{220\}^*$ satellite reflections is not homogeneous and abruptly alters on the 100–200 Å scale. Note that dark regions in such images correspond to zero amplitude of the corresponding $\frac{1}{4}\{220\}^*$ modulation wave.

In addition to the striking reduction in intensity of the $\mathbf{G}_F \pm \frac{1}{4}\{220\}^*$-type satellite reflections from the C-type to the defect fluorite side of the two-phase region (see Fig. 2 of (8)), it has long been known that the satellite reflections on the defect fluorite side of the two-phase region show

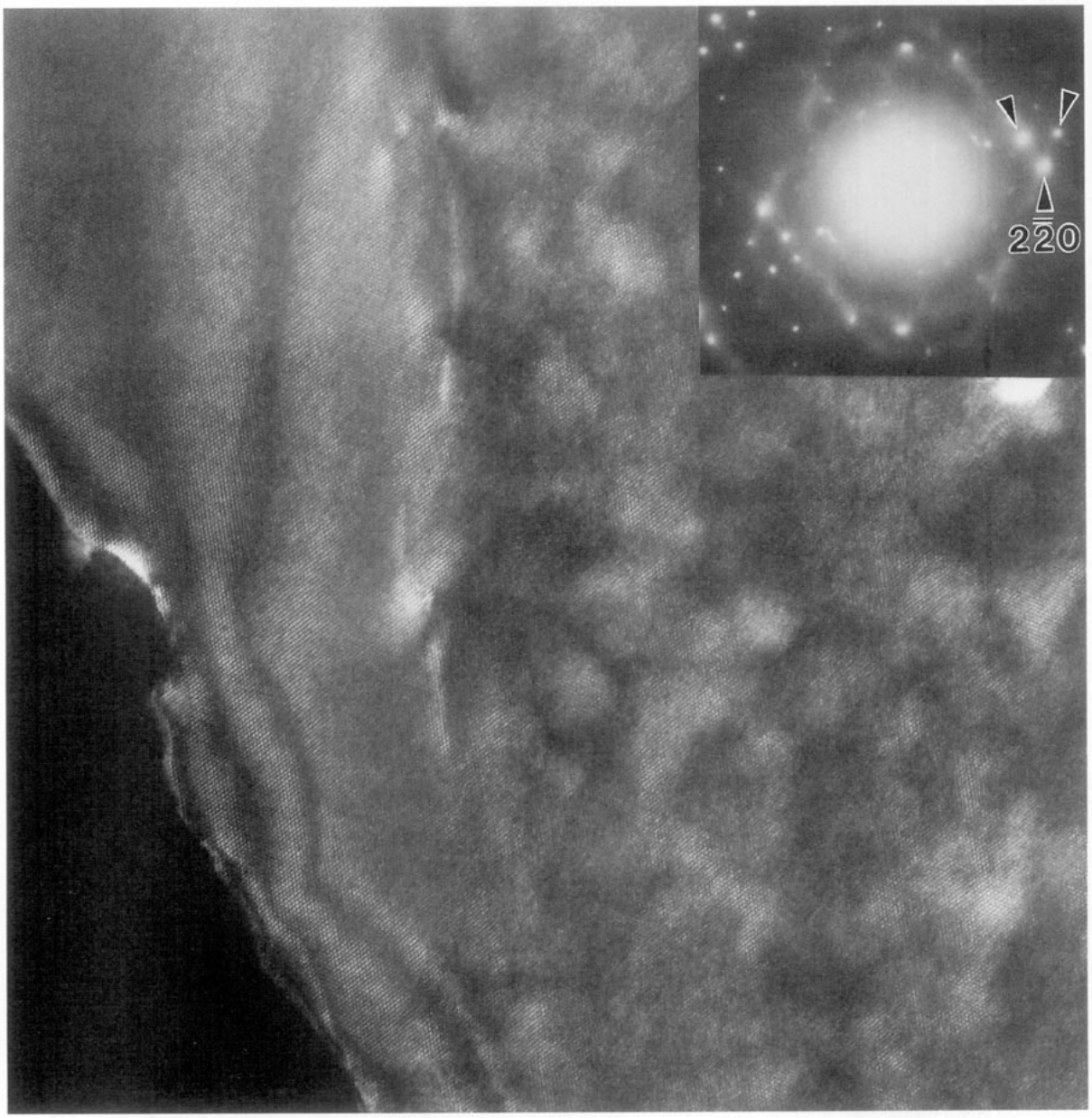

FIG. 4. A higher resolution SDF image of another grain from the 64.8 mole% $YO_{1.5}$ in CeO_2 specimen, showing both C-type (on the left) and defect fluorite (on the right) regions. The corresponding electron diffraction pattern (inset in the top right-hand corner) is relatively close to ⟨111⟩ and obtained by tilting ~5–10° away from ⟨111⟩ in such a way as to keep a $\{2\bar{2}0\}^*$ systematic row excited.

significant peak broadening (see, for example, (9)). This is also qualitatively evident from electron diffraction patterns such as those shown in Fig. 1. In the case of the 49.7 mole% $YO_{1.5}$ in CeO_2 specimen, the full width at half maximum height (FWHM) of the $\mathbf{G}_F \pm \frac{1}{4}\{220\}^*$-type satellite reflections (in particular, the FWHM of the $\{111\}^*-\frac{1}{4}\{022\}^*$ satellite reflection—see Fig. 2 of (8)) in powder XRD patterns has been used to estimate the average domain size, i.e., the average diameter of a microdomain, to be ~140 Å. The effects of instrumental broadening were taken into account by measuring the FWHM of several parent fluorite Bragg reflections and led to the average domain size estimate increasing from 130 to 140 Å. Such an average domain size estimate is in good agreement with the scale of the microstructure visible in Figs. 2b and 3b. Annealing specimens at temperatures of 1000–1200°C for periods of up to 2 weeks were found to have negligible effect upon the microstructure scale as estimated from such SDF imaging.

The FWHM of the $\mathbf{G}_F \pm \frac{1}{4}\{220\}^*$-type satellite reflections

on the C-type sides of such two-phase regions, however, are as sharp as the average fluorite parent reflections and suggest that the correlation lengths of the $\frac{1}{4}\{220\}^*$ modulation waves on the C-type side must be $>\sim$ 1000 Å, i.e., the $\frac{1}{4}\{220\}^*$ modulation waves on the C-type side of such two-phase regions are essentially long-range ordered. This is strikingly confirmed by $\mathbf{G}_F \pm \frac{1}{4}\{220\}^*$ SDF images taken of specimens grown within the two-phase region such as that from the 64.8 mole% $YO_{1.5}$ in CeO_2 specimen shown in Fig. 3b and taken tilted ~5–10° away from an ⟨001⟩ zone axis orientation. (A back-scattered electron image of the same specimen in Fig. 3a shows that the sample has unmixed on the micrometer scale. The darker regions in Fig. 3a correspond to the ~73 mole% $YO_{1.5}$, C-type side of the two-phase region, whereas the lighter regions correspond to the ~50 mole% $YO_{1.5}$, defect fluorite side of the two-phase region.) The right-hand side of the grain in Fig. 3b corresponds to the C-type side of the two-phase region and shows absolutely no evidence for a microdomain texture, whereas the left-hand side of the grain corresponds to the defect fluorite side of the two-phase region and shows clearly the existence of microdomains on the 100–200 Å scale. The strain associated with the slightly different underlying fluorite-type cell parameters on either of the two-phase regions is taken up by what appear to be a network of misfit dislocations. Such images are again also characteristic of the $(1 - x)ZrO_2.xRO_{1.5}$, R = Ho, Dy, Tb, and Gd, specimens grown within the two-phase region.

A higher resolution dark field image of another grain from the same specimen, also showing both C-type (on the left) and defect fluorite (on the right) regions, is shown in Fig. 4. The corresponding electron diffraction pattern (inset in the top right-hand corner of Fig. 4) is relatively close to ⟨111⟩ and obtained by tilting ~5–10° away from ⟨111⟩ in such a way as to keep a $\{2\bar{2}0\}^*$ systematic row excited. The objective aperture used was centered on the three strongly excited reflections arrowed in the diffraction pattern corresponding to the $\{2\bar{2}0\}^*$ parent fluorite reflection as well as the $\{2\bar{2}0\}^* + \frac{1}{4}\{02\bar{2}\}^*$ and $\{2\bar{2}0\}^* - \frac{1}{4}\{\bar{2}02\}^*$ satellite reflections. The interference between these three beams gives rise to the $4a_F/\sqrt{8} \sim 7.3$ Å, approximately hexagonal set of fringes clearly visible over almost all the field of view in the left-hand or C-type region on Fig. 4.

The intriguing feature of the right-hand or defect fluorite region of the image is that the relative visibility of these fringes often abruptly alters on the microdomain scale of ~100–200 Å so that there are regions where all three sets of fringes are strongly excited (corresponding as would be expected to the brighter parts of the defect fluorite region of the image), regions where one or other set of fringes are rather more strongly excited than the other two sets of fringes and regions where none of the sets of fringes are strongly excited. It should be borne in mind, given the small size and irregular shape of the microdomains, that the incident electron beam is highly likely to be traversing more than one microdomain before emerging from the crystal and hence the observed contrast is not trivial to interpret. Nonetheless it is quite clear that both the absolute as well as relative amplitudes of the $\frac{1}{4}\{02\bar{2}\}^*$ and $\frac{1}{4}\{\bar{2}02\}^*$ modulation waves can vary quite abruptly on the 100–200 Å scale. That both $\frac{1}{4}\{02\bar{2}\}^*$ and $\frac{1}{4}\{\bar{2}02\}^*$ modulation waves do not necessarily have the same amplitude at any one point automatically implies that the local space group symmetry must be lower than cubic *Ia3*. Cubic *Ia3* space group symmetry necessarily requires all size $\frac{1}{4}\{220\}^*$-type modulation waves to coexist locally (13). The exact local symmetry, however, is rather difficult to determine experiment as a result of the small microdomain size, the irregular shape of the boundaries, and the fact that only three of the six possible $\mathbf{G}_F \pm \frac{1}{4}\{220\rangle^*$-type satellite reflections can ever be simultaneously excited in the zero order laue zone (ZOLZ) at any one zone axis orientation.

DISCUSSION

The absence of $\mathbf{G}_F \pm \frac{1}{4}\{220\}^*$-type satellite reflections in the ZOLZ of ⟨001⟩ zone axis electron diffraction patterns on either side of the two-phase region, as shown previously, requires that $\frac{1}{4}\{220\}^*$ modulation waves can only be associated with oxygen vacancy ordering and associated structural relaxation (13). The latter relaxation can be thought of as a response to the primary variable—the oxygen vacancy distribution. The question becomes—what is the nature of the local oxygen vacancy distribution on either side of the two-phase region and what is the change in its fundamental character that gives rise to the observed two-phase region?

The absence of contrast in satellite dark field images on the C-type side of the two-phase region shows that the nature of the local oxygen vacancy distribution on this side of the two-phase region is that characteristic of the well-known end-member C-type sesquioxide structure itself (see (8)). This structure (of *Ia3*, $a_C = 2a_F$, space group symmetry) has the oxygen vacancies arranged such that there are no $\frac{1}{2}\langle 100\rangle$ oxygen vacancy pairs around filled metal atom sites. Due to the large proportion (25%) of oxygen vacancies, however, it allows $\frac{1}{2}\langle 110\rangle$ vacancy pairs around filled metal atom sites and $\frac{1}{2}\langle 111\rangle$ oxygen vacancy pairs across empty cubes.

What is the nature of the local oxygen vacancy distribution on the defect fluorite side of the two-phase region and why can this local order not extend beyond ~55 mole% $RO_{1.5}$? One possible approach is suggested by a recent detailed study of the complex diffuse X-ray scattering patterns obtained from an yttria-stabilized cubic zirconia of composition $Zr_{0.61}Y_{0.39}O_{1.805}$, i.e., $x = 0.39$ (15, 16). In these studies it was found that the model which best fits the

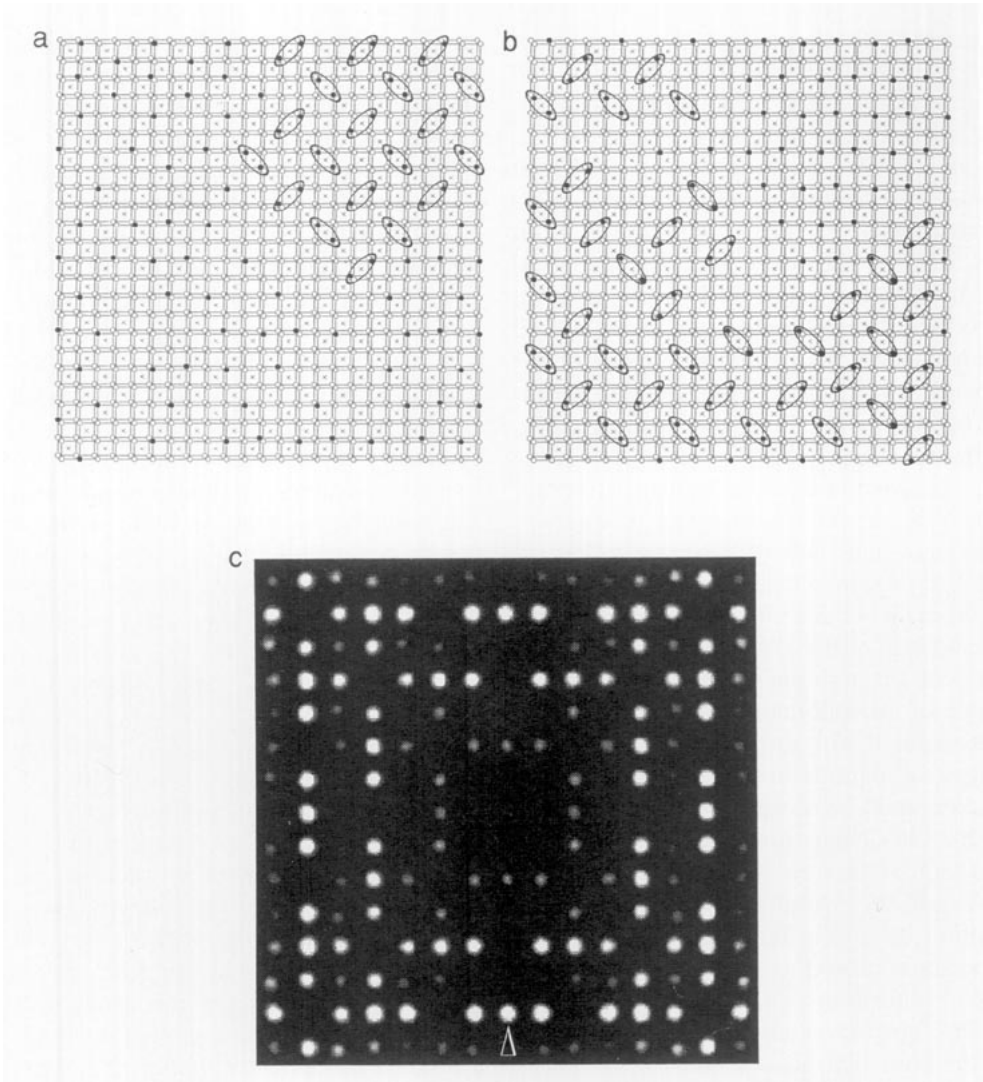

FIG. 5. (a) and (b) show the oxygen vacancy distribution generated in two successive layers of the average fluorite structure at an oxygen vacancy concentration of 10.4% by application of the local rules for oxygen vacancy ordering described in the text. Ellipses are drawn around $\frac{1}{2}\langle 111\rangle$ vacancy pairs. The cation sites are indicated by a cross. Ordering of the $\frac{1}{2}\langle 111\rangle$ oxygen vacancy pairs into microcrystals of a *Pa3*, $a_s = 2a_F$, ordered oxygen vacancy distribution is clearly visible. The corresponding h, k, 0.5 section of reciprocal space is shown in (c). The arrowed reflection corresponds to $(3, 0, \frac{1}{2})^* = (200)^* + \frac{1}{2}(201)^*$.

observed scattering patterns was one in which the oxygen vacancies order in such a way as to avoid nearest neighbour $\frac{1}{2}\langle 100\rangle$ pairs, next nearest neighbour $\frac{1}{2}\langle 110\rangle$ pairs, and third nearest neighbour $\frac{1}{2}\langle 111\rangle$ pairs across empty cubes of oxygens, but encouraged third nearest neighbour $\frac{1}{2}\langle 111\rangle$ pairs across cubes of oxygens containing the cations (16). (Such local oxygen vacancy ordering rules are compatible with most (17), although not all (18), known fluorite-related superstructure phases.) In order to fit the observed diffuse distribution more accurately, it was also found to be necessary to strongly suppress the tendency for the allowed $\frac{1}{2}\langle 111\rangle$ vacancy pairs to form $\langle 110\rangle$ chains as in the pyrochlore structure (16).

At the 9.75% oxygen vacancy concentration of $Zr_{0.61}Y_{0.39}O_{1.805}$, the above local rules are insufficient to generate ordered oxygen vacancy superstructures. As the oxygen vacancy concentration increases, however, toward 12.5% at $x = 0.50$, these local rules begin to generate microcrystals of a *Pa3*, $a_P = 2a_F$, ordered oxygen vacancy distribution (see Fig. 5 and (8)). Figures 5a and 5b, for example, show the oxygen vacancy distribution generated in two successive layers by application of the above local rules and for an oxygen vacancy concentration of 10.4% (compare with Fig. 7c of (8)). Such microcrystals give rise to $\mathbf{G}_F \pm \frac{1}{4}\{220\}^*$-type satellite reflections as required. Unfortunately, however, they also generate unobserved $\mathbf{G}_F \pm \frac{1}{2}\{201\}^*$-type satellite reflections (see Fig. 5c). It was suggested in (8) that these unwanted satellite reflections

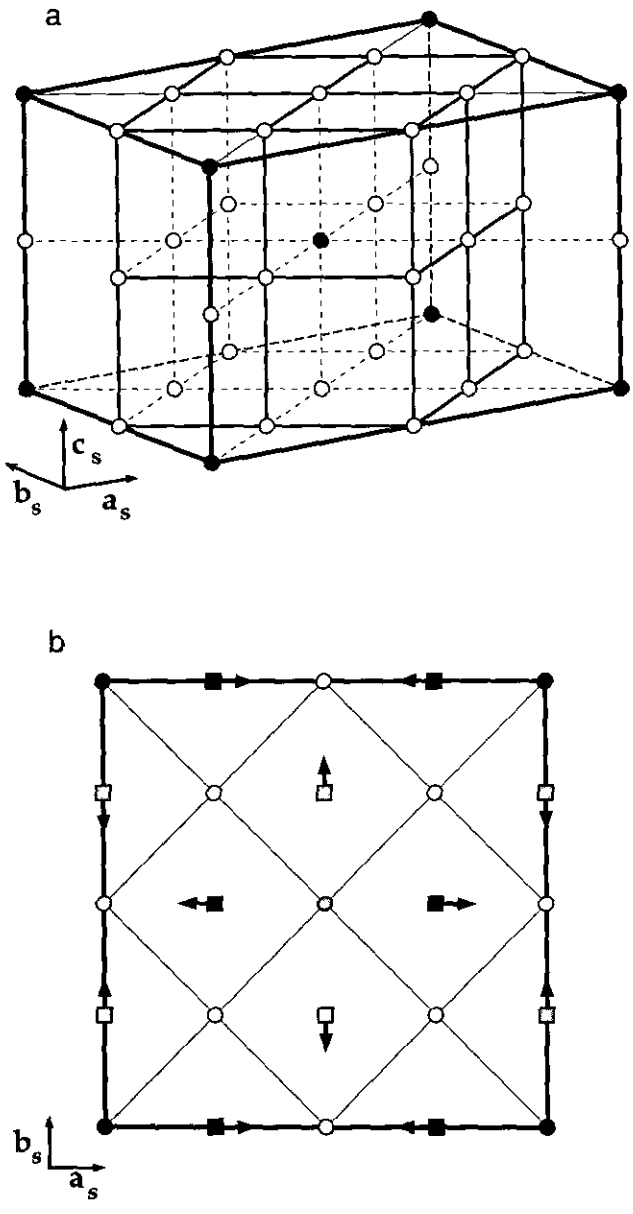

FIG. 6. (a) A perspective drawing of a possible oxygen vacancy ordering scheme which, locally, gives rise to some, but not all, of the six possible $\mathbf{G}_F \pm \frac{1}{4}\{220\}^*$-type satellite reflections. For clarity, only the oxygen sites are shown (vacancies are indicated by a filled circle whereas occupied sites are indicated by an open circle). The resultant supercell is indicated in bold type. The cation shifts that would accompany such an oxygen vacancy distribution are shown in (b) in projection along $\mathbf{c}_s = \mathbf{c}_F$. Cation sites are indicated by squares (filled squares and hatched squares are at different heights along $\mathbf{c}_s$).

could possibly be removed if $\frac{1}{2}\langle 111\rangle_p = \langle 111\rangle$ stacking faults occurred on a fine enough, i.e., ~100–300 Å, scale. The SDF images of Figs. 2–4, however, unequivocally rule out any model which has all six $\frac{1}{4}\{220\}^*$-type modulations simultaneously locally excited, i.e., any model, such as the above *Pa3* model, which has local cubic symmetry.

An oxygen vacancy ordering pattern is needed for $x \sim 0.5$ which, locally, gives rise to some, but not all, of the six possible $\mathbf{G}_F \pm \frac{1}{4}\{220\}^*$-type satellite reflections. One such possible oxygen vacancy ordering scheme is shown in Fig. 6a. The oxygen vacancy concentration is 12.5%, corresponding to $x = 0.50$. Note that the oxygen vacancies in this model occur as isolated vacancies rather than as $\frac{1}{2}\langle 111\rangle$ vacancy pairs and that these isolated vacancies are separated by $\frac{1}{2}\langle 201\rangle$. When the cation shifts that would be expected to accompany such an oxygen vacancy distribution are included (see Fig. 6b), the resultant local space group symmetry is tetragonal $P4_2/nmc$ with $\mathbf{a}_s = \mathbf{a}_F + \mathbf{b}_F$, $\mathbf{b}_s = -\mathbf{a}_F + \mathbf{b}_F$, and $\mathbf{c}_s = \mathbf{c}_F$. The corresponding reciprocal space unit cell vectors are $\mathbf{a}_s^* = \frac{1}{4}(220)^*$, $\mathbf{b}_s^* = \frac{1}{4}(\bar{2}20)^*$, and $\mathbf{c}_s^* = (001)^*$, i.e., only two of the six possible $\mathbf{G}_F \pm \frac{1}{4}\{220\}^*$-type satellite reflections would be generated locally by such a model. There exist three possible orientations for the unique tetragonal axis corresponding to the **a**, **b**, and **c** directions of the underlying fluorite-type substructure and hence three distinct microdomains would be expected.

Such a model is entirely compatible with the experimental results presented in this paper. Whether it is the only possible model, however, remains unclear. If confirmed, it suggests that the notion that $\frac{1}{2}\langle 111\rangle$ vacancy pairs across a metal site should be a common structural element in any oxygen-deficient, fluorite-related system is, in fact, not correct and that the structural principal underlying the existence of defect fluorite-type solid solutions still remains unknown. The recently reported structure of $Tb_{11}O_{20}$ (18) led the authors of that paper to a similar conclusion.

While we cannot claim to have unambiguously determined the exact nature of the ordering on the defect fluorite side of the two-phase region, it is nonetheless clear that there is a definite symmetry change associated with moving across the two-phase region, that the defect fluorite side of the two-phase region is characterized by a microdomain texture on the ~100–200 Å scale and that the local symmetry within any one of these microdomains is clearly lower than cubic.

REFERENCES

1. A. Rouanet, *Rev. Int. Hautes Temp. Réfract.* **8,** 161 (1971).
2. J. D. McCullough and J. D. Britton, *J. Am. Chem. Soc.* **74,** 5225 (1952).
3. G. Brauer and H. Gradinger, *Naturwiss* **38,** 559 (1951).
4. R. Wallenberg, R. L. Withers, D. J. M. Bevan, J. G. Thompson, P. Barlow, and B. G. Hyde, *J. Less-Common Met.* **156,** 1 (1989).
5. S. Suzuki, M. Tanaka, and M. Ishigame, *Jpn. J. Appl. Phys.* **24,** 401 (1985).
6. R. L. Withers, J. G. Thompson and P. Barlow, *J. Solid State Chem.* **94,** 89–105 (1991).
7. R. L. Withers, J. G. Thompson, and J. C. Barry, *J. Comput. Assisted Microsc.* **4,** 315–317 (1992).

8. N. Gabbitas, J. G. Thompson, R. L. Withers, and A. D. Rae, *J. Solid State Chem.* **115,** 23–36 (1995).
9. D. J. M. Bevan, W. W. Parker, T. C. Parks and R. L. Martin, *in* "Rare Earth Research" (L. Eyring, Ed.), p. 441. Gordon and Breach, New York (1965).
10. M. Thornber, D. J. M. Bevan, and E. Summerville, *J. Solid State Chem.* **1,** 545 (1970).
11. D. J. M. Bevan and E. Summerville, *in* "Handbook on the Physics and Chemistry of Rare Earths" (K. A. Gschneider and L. Eyring, Eds), Vol. 3, p. 421 North-Holland, Amsterdam (1979).
12. B. G. Hyde, D. J. M. Bevan, and L. Eyring, *Philos. Trans. Royal Soc. London Ser. A* **259,** 583 (1966).
13. R. L. Withers, R. Wallenberg, D. J. M. Bevan, J. G. Thompson, and B. G. Hyde, *J. Less-Common Met.* **156,** 17 (1989).
14. S. Suzuki, M. Tanaka, and M. Ishigame, *Jpn. J. Appl. Phys.* **26,** 1983 (1987).
15. T. R. Welberry, R. L. Withers, J. G. Thompson, and B. D. Butler, *J. Solid State Chem.* **100,** 71–89 (1992).
16. T. R. Welberry, B. D. Butler, J. G. Thompson, and R. L. Withers, *J. Solid State Chem.* **106,** 461–475 (1993).
17. H. J. Rossell and H. G. Scott, *J. Phys. Colloq.* **38**(C7), 28–31 (1977).
18. J. Zhang, R. B. Von Dreele and L. Eyring, *J. Solid State Chem.* **104,** 21–32 (1993).